Available online at www.sciencedirect.com
SCIENCE DIRECT®
European Journal of Mechanics B/Fluids 25 (2006) 59–73

# The effect of an insoluble surfactant on the skin friction of a bubble

Jie Li

*BP Institute and Engineering Department, University of Cambridge, UK*

Received 6 September 2004; received in revised form 17 February 2005; accepted 20 April 2005

Available online 17 May 2005

**Abstract**

In this paper, we develop a novel moving mesh method suitable for solving axisymmetric free-boundary problems, including the Marangoni effect induced by surfactant or temperature variation. This method employs a body-fitted grid system where the gas–liquid interface is one line of the grid system. We model the surfactant equation of state with a non-linear Langmuir law, and, for simplicity, we limit ourselves to the situation of an insoluble surfactant. We solve complicated dynamic boundary conditions accurately on the gas–liquid interface in the framework of finite-volume methods. Our method is used to study the effect of a surfactant on the skin friction of a bubble in a uniaxial flow. For the limiting case where the surface diffusivity is zero, the effect of a tangential stress generated by the surface tension gradient, allows us to explain a new phenomenon in high concentration regimes: larger surface tension, but also larger deformation. Furthermore, this condition leads to the formation of boundary layers and flow separation at high Reynolds numbers. The influence of these complex flow patterns is examined.


*Keywords:* Interface tracking; Moving mesh method; Free-surface problem; Surfactant; Langmuir state equation; Skin friction; Marangoni effect; Flow separation

## 1. Introduction

Surfactants are “impurities” such as soap, detergent and food grease, which form a kind of skin on the surface of a liquid. They can prolong the merging rate of liquid droplets hundreds of times [1] and significantly reduce the bubble rising speed in liquid [2–4]. Effects of surfactants are important in bio-mechanical flows. For example, some insects drift on water by injecting a chemical at the rear. This chemical reduces the surface tension behind their bodies so that the insects are pulled forward. Another example is the airway reopening flow, where the air has to enter the fluid-filled airways in the lung of a newborn baby for the first time. This work is part of our effort to incorporate complicated physics involving moving boundaries in a general and flexible framework, where we have included useful abilities, such as handling a viscoelastic fluid and the Marangoni effect induced from the variation of surfactant concentration on the liquid surface.

To deal with the difficult free-boundary problems with surfactant phenomena, we develop a novel ALE (Arbitrary Lagrangian Eulerian) moving mesh method. This method employs velocity and pressure as computational variables and a body-fitted grid system where the gas–liquid interface is one line of the grid system. Based on a Finite-Volume formulation, complicated dynamic boundary conditions are incorporated naturally and accurately in our method [5]. The resulting non-linear system of mass and momentum conservation is solved by a projection method. The efficiency of the our solver is guaranteed by a multigrid grid method, solving the pressure equation. Finally, we use a finite volume scheme to solve for surfactant transport on the interface. The virtue of this scheme is that it conserves exactly the total surfactant at every time step. The gas–liquid interface is represented by a series of ordered marker points and a continuously smooth parametrization of the interface is obtained through a cubic spline of these points.

0997-7546/$ – see front matter 
doi:10.1016/j.euromechflu.2005.04.002

Our numerical method is used to investigate the effect of increasing skin friction on the bubble deformation and breakup in uniaxial extensional flow. This problem has attracted the attention of many researchers since G.I. Taylor. One of the well-known problems is the bubble deformation and breakup in uniaxial extensional flow. Previous numerical studies on this flow problem have been restricted to the case of constant surface tension [6]. However, in many practical situations, the gas–liquid interface is not clean; surfactant may be adsorbed to the surface and alters the surface tension there. Since the stress balance of the gas–liquid surface depends upon the surface tension, the surfactant concentration on the surface has an important impact on the bulk flow in many situations. In particular, non-uniform surfactant concentration produces a gradient of the surface tension along the interface, and modifies the tangential interfacial stress balance. This phenomenon is the so-called Marangoni effect.

For simplicity, we limit ourselves to the situation of an insoluble surfactant. The surface diffusivity of the surfactant is a critical factor for the physical phenomena observed. Typically, surface diffusion is extremely weak. In all this work, we set $D_s = 0$. Our choice of $D_s$ is of relevance, and it reveals new physical phenomena which have not been investigated by the previous authors. It will allow us to resolve a paradox in high concentration regimes: larger surface tension, but also larger deformation. Furthermore, at high Reynolds numbers, the non-slip condition leads to rich flow patterns, and thus we have the opportunity to examine the effect of boundary layers and flow separation from bubble surface. In this work, we investigate the effect of the surfactant on the bubble deformation for Reynolds number between $Re = 10$ and 1000.

## 2. Governing equations

The free-surface problems involving the Marangoni effect induced by surfactant or temperature variation are often highly non-linear processes. We shall compute these flows numerically. We assume that the density and viscosity of the gas inside the gas phase are negligible in comparison with those of the liquid. Finally, we consider the situation where the gas–liquid interface surface is covered with surfactant of undisturbed concentration $\Gamma_0$. The surface tension $\gamma$ varies with local surfactant concentration $\Gamma$. In this work, the surfactant is assumed to be insoluble in the liquid phase so that the convection and diffusion of surfactant are neglected in the bulk. The case of insoluble surfactant corresponds to the physical situation where the time scale for surfactant adsorption is very slow compared to convection. The surfactant acts in general to lower the surface tension. We use a non-linear Langmuir model [3,4] to determine the surfactant equation of state:

$$\gamma = \gamma_s + RT\Gamma^\infty \ln\left(1 - \frac{\Gamma}{\Gamma^\infty}\right), \tag{1}$$

where $\gamma_s$ is the surface tension of a clean interface, $R$ the gas constant, $T$ the temperature, and $\Gamma^\infty$ the saturated concentration. In (1), as the local concentration $\Gamma$ approaches the saturated concentration $\Gamma^\infty$, the work required to compress the surface diverges logarithmically. As a warning note, at very high concentrations, the validity of the Langmuir equation cannot be taken for granted, and any conclusions obtained through this equation must be regarded cautiously. The equation governing the concentration of an insoluble surfactant on the interface reads [7,8]:

$$\frac{\partial \Gamma}{\partial t} + \nabla_s \cdot (u_t \Gamma) + \kappa u_n \Gamma = D_s \nabla_s^2 \Gamma, \tag{2}$$

where $u_n$ and $u_t$ are normal and tangential velocities on the surface, $D_s$ the surface diffusivity, and $\nabla_s$ is the surface gradient operator. The third term of the equation is due to the contraction and stretching of the interface, where $\kappa$ is the local surface curvature.

We consider a Newtonian liquid in this work. The fluid motion is governed by the incompressible Navier–Stokes equations. Under the assumption of axisymmetry, the continuity equation is

$$\frac{\partial u}{\partial z} + \frac{1}{r}\frac{\partial}{\partial r}(rv) = 0, \tag{3}$$

and the momentum equations

$$\frac{\partial u}{\partial t} + u\frac{\partial u}{\partial z} + v\frac{\partial u}{\partial r} = -\frac{\partial p}{\partial z} + \frac{\partial}{\partial z}\left(2\mu\frac{\partial u}{\partial z}\right) + \frac{1}{r}\frac{\partial}{\partial r}\left(r\mu\left(\frac{\partial u}{\partial r} + \frac{\partial v}{\partial z}\right)\right), \tag{4}$$

$$\frac{\partial v}{\partial t} + u\frac{\partial v}{\partial z} + v\frac{\partial v}{\partial r} = -\frac{\partial p}{\partial r} + \frac{\partial}{\partial z}\left(\mu\left(\frac{\partial u}{\partial r} + \frac{\partial v}{\partial z}\right)\right) + \frac{1}{r}\frac{\partial}{\partial r}\left(r(2\mu\frac{\partial v}{\partial r})\right) - \frac{2\mu v}{r^2}, \tag{5}$$

where $u$ and $v$ are the axial and radial velocities, and $p$ the pressure. We consider that the gas is incompressible and has a constant pressure $p_0$. Without loss of the generality, we assume the constant pressure $p_0 = 0$. Hence the dynamic boundary condition on the surface expresses the following balance of forces:

$$(-p\mathbf{I} + \mu\mathbf{D}) \cdot \mathbf{n} = \gamma\kappa\mathbf{n} + \nabla_s\gamma, \tag{6}$$

where **D** is the strain rate tensor, $s$ the arc-length of the interface, **n** the normal vector of the interface and **t** the tangential vector. To complete the problem formulation, we require the kinematic boundary condition on the gas–liquid interface:

$$\frac{\mathrm{d}\mathbf{r}}{\mathrm{d}t} = \mathbf{u}, \quad \text{where } \mathbf{r} = (z, r), \tag{7}$$

which means the interface moves with the speed of the fluid.

## 3. Numerical method

In a moving grid method, by using the so-called boundary-fitted coordinate system, the free surface coincides with one line of the numerical grid. This type of method has the tremendous advantage that the boundary condition can be resolved very accurately. A successful application of the moving grid method depends crucially on the quality of the mesh we can generate. It is an appropriate choice for the flow problem we study in this work, since the interface only undergoes moderate deformation. For the case where the interface undergoes severe deformation, even breakup, a fixed mesh method is more appropriate [9–11]. The boundary condition (Eq. (6)) on the free surface is expressed naturally in term of the primitive variables. This motivates us to develop a new ALE (Arbitrary Lagrangian Eulerian) method, where the spatial discretization of the primitive variables uses a partially staggered approach: the pressure $p$ is defined at the cell center while both Cartesian velocity $u$ and $v$ are defined on the cell corner (see Fig. 1). As shown in Sani and Gresho [5], the dynamic boundary condition can be incorporated naturally and accurately in the ALE method. In fact, from Eq. 6, we replace the stress force $(-p\mathbf{I} + \mu\mathbf{D})\mathbf{n}$ on the surface with the surface tension force $\gamma\kappa\mathbf{n} + \frac{\partial\gamma}{\partial s}\mathbf{t}$ in the finite-volume formulation of the momentum equation. Our numerical method does not require the mesh to be orthogonal; the orthogonality of a mesh is desirable but not easy to obtain in many cases. Our method is therefore flexible.

We solve the Navier–Stokes equation by an explicit projection method [12]. We first work on a fixed mesh for the time $t^n = n\Delta t$. We calculate an approximate velocity $\mathbf{u}^*$ without the pressure gradient $\nabla p$ from the momentum equations, assuming that the velocity $\mathbf{u}^n$ at time $t_n$ is known:

$$\frac{\mathbf{u}^* - \mathbf{u}^n}{\Delta t} = \mathbf{F}(\mathbf{u}^n), \tag{8}$$

where the term $\mathbf{F}(\mathbf{u}^n)$ includes the convection and diffusion terms in the momentum equation. In general, the resulting flow field $\mathbf{u}^*$ does not satisfy the continuity equation. However, we require that $\nabla \cdot \mathbf{u}^{n+1} = 0$ and

$$\frac{\mathbf{u}^{n+1} - \mathbf{u}^*}{\Delta t} = -\nabla p^n. \tag{9}$$

Taking the divergence of Eq. (9), we obtain a Poisson-like equation

$$\nabla \cdot (\nabla p^n) = \frac{\nabla \cdot \mathbf{u}^*}{\Delta t} = \nabla \cdot \big(\mathbf{F}(\mathbf{u}^n)\big). \tag{10}$$

The solution of this equation is determined with appropriate boundary conditions for the pressure. The boundary condition on the free interface is the Dirichlet condition, which is computed from the balance of the normal stress on the free surface

$$p^n = \mathbf{n}(\mu\mathbf{D}^n)\mathbf{n} - \gamma^n\kappa^n. \tag{11}$$

This condition is derived from Eq. 6. As pointed out in Sani and Gresho [5], the time 'index' on $p$ in Eqs. (9) and (10) is perfectly proper; it should not be $p^{n+1}$ as many believe. Eq. (10) is the best equation to use to prove this assertion. The RHS

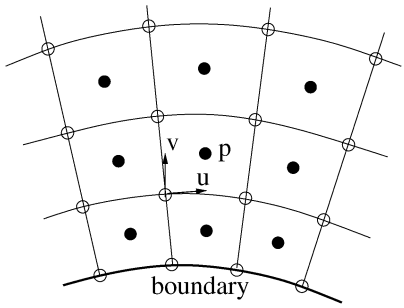


Fig. 1. ALE mesh. The pressure $p$ is defined at the cell center while both Cartesian velocities $u$ and $v$ are defined on the cell corner.

of Eq. (10) and the Dirichlet boundary condition equation (11) are completely determined by terms at the time step $n$, and we should not forget that the mesh we use here is still the one at the time step $n$. The solution of the discrete counterpart of Poisson's equation (10) is the most time-consuming part of our Navier–Stokes solver and, consequently, an efficient solution is crucial for the performance of the whole method. The multigrid method is arguably the most efficient method: to reduce the error in the discretization of Poisson's equation by a constant, the multigrid method requires a fixed number of iterations, independent of the mesh size. Our multigrid method was developed in Li [13], Chapter 6.

We remind the reader that until now we have worked on the mesh at time $t^n$. From Eq. (9), we compute the velocity field for the time $t^{n+1}$ on this same mesh. We then compute the new free surface through the Lagrangian formula

$$\mathbf{x}^{n+1} = \mathbf{x}^n + u_n \mathbf{n}(\Delta t) \tag{12}$$

using the normal component of velocity. Finally, we generate a new mesh $\mathbf{x}^{n+1}$ which fits the new free surface. The velocity field on the new mesh is extrapolated through

$$\mathbf{u}^{n+1}(\mathbf{x}^{n+1}) = \mathbf{u}^{n+1}(\mathbf{x}^n) + (\mathbf{x}^{n+1} - \mathbf{x}^n) \cdot \nabla \cdot (\mathbf{u}^{n+1})(\mathbf{x}^n). \tag{13}$$

This step can also be interpreted from the composite rule of derivatives

$$\frac{\mathrm{d}\mathbf{u}}{\mathrm{d}t} = \frac{\partial \mathbf{u}}{\partial t} + \mathbf{v}\nabla\mathbf{u}, \tag{14}$$

where $\mathbf{v}$ is the mesh motion speed. It is worthwhile to note that the new velocity field is no longer divergence free, but this does not induce numerical difficulties.

In our method, the interface is represented by a series of marker points $\mathbf{r}_i$, $i = 1, \ldots, N$, on the surface. A cubic spline is used to obtain a continuous smooth parametrization of the surface and compute accurately the surface curvature. We use a fractional step approach to solve the transport of the surfactant on the surface. We first solve the tangential part of the increment of surfactant:

$$\frac{\partial \Gamma}{\partial t} + \nabla_s \cdot (u_t \Gamma) = D_s \nabla_s^2(\Gamma), \tag{15}$$

using a finite volume method [14]. Since the second order central scheme is unconditionally unstable when $D_s = 0$, the first order upwind scheme is used to compute the convective flux. In a first order method, the concentration distribution is represented as a constant function on each surface element. Let us denote the average concentration on a surface element $[\mathbf{r}_i, \mathbf{r}_{i+1}]$ as $\Gamma_{i+1/2} = \int_{\mathbf{r}_i}^{\mathbf{r}_{i+1}} \Gamma \,\mathrm{d}S / \Delta S_{i+1/2}$, where $\Delta S_{i+1/2}$ is the surface area of the element. Then $\Gamma_{i+1/2}$ increases according to

$$\frac{(\Gamma_{i+1/2}^{n+1} - \Gamma_{i+1/2}^{n})\Delta S_{i+1/2}}{\Delta t} + (r u_t \Gamma)_{i+1}^n - (r u_t \Gamma)_i^n = D_s \left( \left( r \frac{\partial \Gamma}{\partial s} \right)_{i+1}^n - \left( r \frac{\partial \Gamma}{\partial s} \right)_i^n \right). \tag{16}$$

The second step concerns the surface motion in the normal direction. Since we move the interface marker points with their normal velocity (see Eq. (12)), the total surfactant in each surface element $\int_{\mathbf{r}_i}^{\mathbf{r}_{i+1}} \Gamma \,\mathrm{d}S$ does not change at this step. We compute the new average concentration $\Gamma_{i+1/2} = \int_{\mathbf{r}_i}^{\mathbf{r}_{i+1}} \Gamma \,\mathrm{d}S / \Delta S_{i+1/2}$ since we now know the new surface area $\Delta S_{i+1/2}$. The whole scheme conserves the surfactant exactly and no rescaling of surfactant is needed to maintain the total amount of surfactant constant.

## 4. Validation

Our method is validated on the bubble deformation and breakup in uniaxial extensional flow. We consider a gas bubble with undisturbed radius $a$ placed in an uniaxial extensional flow of fluid with constant density $\rho$ and viscosity $\mu$ (see Fig. 2). If the $x$-axis of the cylindrical coordinates $(x, r, \phi)$ is directed along the axis of the symmetry, the velocity field far from the bubble is given by

$$\mathbf{u} = \mathbf{G} \cdot \mathbf{r}, \quad \mathbf{G} = G \begin{pmatrix} 1 & 0 & 0 \\ 0 & -\frac{1}{2} & 0 \\ 0 & 0 & -\frac{1}{2} \end{pmatrix}, \quad G > 0. \tag{17}$$

where $G$ is the principal strain rate.

One of the most important dimensional parameters is the Reynolds number $Re = 2\rho(Ga)a/\mu$, based on the equivalent diameter $2a$ of the bubble, and the characteristic velocity $Ga$. For inertially-dominated flow, the bubble deformation is well characterized by the ratio of inertial forces to capillary forces, which is the Weber number $We = 2\rho(Ga)^2 a/\gamma_0$, where $\gamma_0$ is

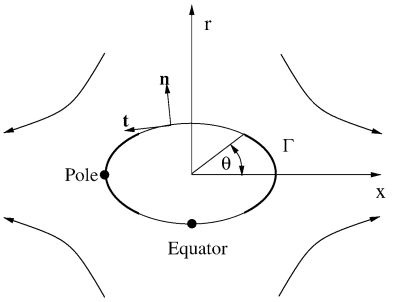


Fig. 2. A bubble placed in a uniaxial flow, and a stagnant cap configuration, where $\Gamma > 0$ and $u_t = 0$ on the thick interface line and $\Gamma = 0$ and $|u_t| > 0$ elsewhere. $\theta$ is the angle of the stagnant cap, **n** the normal vector of interface and **t** the tangential vector.

the surface tension related to the undisturbed surfactant concentration $\Gamma_0$. On the other hand, for inertia-free flow, the bubble deformation is well characterized by the ratio of viscous stresses to capillary forces, which is the Capillary number $Ca = We/Re = \mu Ga/\gamma_0$.

Surfactant diffusion is characterized by the surface Péclet number

$$Pe_s = 2(Ga)a/D_s. \tag{18}$$

Typically, surface diffusion is extremely weak. In this study, we neglect the surface diffusion term and set $D_s = 0$. Therefore $Pe = \infty$. In this condition, the surfactant profile for a steady solution has a strict stagnant cap configuration. In fact, for a steady solution, we obtain from Eq. (2),

$$\nabla_s \cdot (u_t \Gamma) = 0 \quad \text{or} \quad u_t \Gamma = \text{constant}. \tag{19}$$

This constant is zero at the stagnant points, therefore

$$u_t = 0 \quad \text{or} \quad \Gamma = 0. \tag{20}$$

In fact, during the flow, the surfactant is convected toward the two poles and produces a surface tension gradient which is exactly balanced by the viscous stress.

The sensitivity of the surface tension to the variation of concentration $\Gamma$ is an important parameter, and is measured by the *Elastic* number

$$E = \frac{RT\Gamma^\infty}{\gamma_0}. \tag{21}$$

Finally, we normalize surfactant concentration with respect to the saturation concentration. This is denoted by

$$x = \frac{\Gamma}{\Gamma^\infty}. \tag{22}$$

We consider a broad range of the surface coverage $x$ ($x$ ranging from an extremely dilute value 0.01 to an extremely concentrated value 0.996). These values can be assumed in practice. In this work, we set the value of $E$ to 0.2.

We compute only steady solutions in this work. Steady solutions are obtained by marching along the time until the normal velocity on the interface is very small (typically $|\mathbf{u} \cdot \mathbf{n}| < 10^{-4}$) at each marker point and the surface concentration at each surface element changes by a negligible amount between two time steps (typically less than $10^{-5}$). We first validate our method against the wealth of results on bubble dynamics without surfactant. We investigated the shapes of a bubble in uniaxial flow as a function of Weber number *We* for Reynolds number $Re = 0.1$ and 100. Our solutions are in good agreement with the well-known results obtained by the stream-function and vorticity formulation [6]. Additional validation of the method can be found in M. Hesse's MPhil thesis [15] on the rising bubble problem. These results are close to identical to the numerical results of Ryskin and Leal [16]. The slight difference between the two results may be attributed to the difference between the meshes.

The new feature of our numerical method is the capability to deal with a free-surface with surfactant phenomena. There are few results regarding bubble dynamics with surfactant. We first evaluate the convergence of the numerical method for the concentration profile for two cases: (1) $Re = 10$, $We = 0.5$ and $x = 0.1$, and (2) $Re = 1000$, $We = 0.5$ and $x = 0.01$. The concentration profile for case 1 is computed on five different meshes and shown in Fig. 3. In this diagram, the solid lines represent the profile on a high resolution mesh $64 \times 256$, while each figure illustrates the defect of lower resolution meshes as indicated in the caption. We note that the second dimension of the mesh size is the number of grid points on the interface. Both here and in what follows, the arclength $s$ along the surface, starting from a tip of the bubble and ending at the equator, is normalized by the total length along the surface. This allows us to compare profiles realized on bubbles of different lengths in

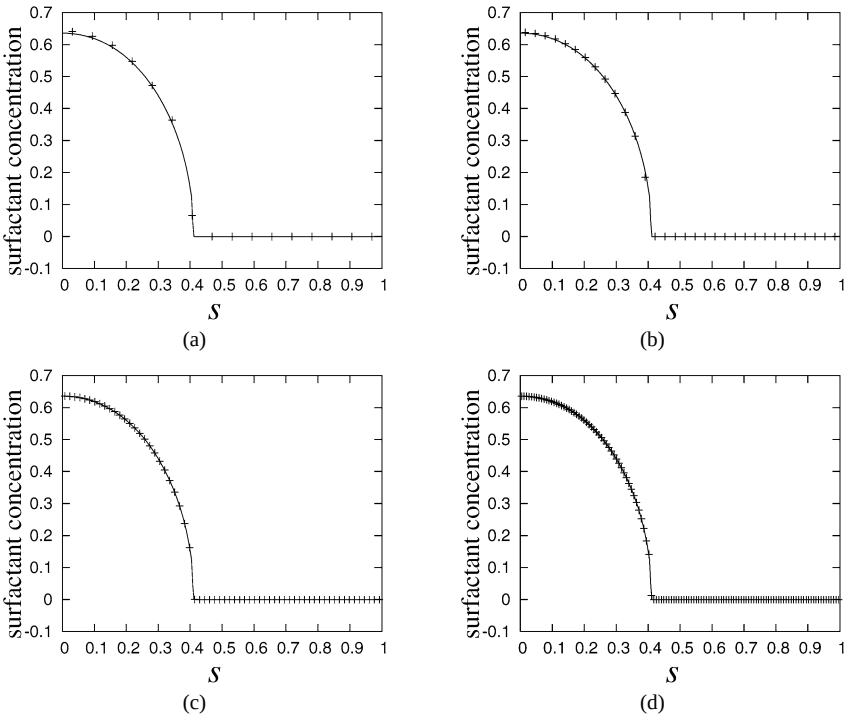


Fig. 3. Convergence of the concentration profile for $Re = 10$, $We = 0.5$ and $x = 0.1$. The solid line represents the profile computed on a $64 \times 256$ mesh. The '+' symbol represents the profile computed on a $32 \times 16$ in (a), $32 \times 32$ in (b), $64 \times 64$ in (c), and $64 \times 128$ in (d).

a single graph. In order to evaluate the convergence in precise terms, we compute the convergence on the normalized $L^1$ norm defined as

$$\|\hat{x} - x\|_{L^1} = \frac{\int_0^1 |\hat{x} - x| \, \mathrm{d}s}{\int_0^1 |x| \, \mathrm{d}s} \tag{23}$$

where $x$ is the exact solution and $\hat{x}$ an approximation. Since we do not know the analytical profile for this problem, we use the profile computed on the mesh $64 \times 256$ as the profile of reference. The first order convergence of our computation is clearly demonstrated in Fig. 4. The solid line represents first order convergence, while the '+' symbol represents the $L^1$ norm error as function of the inverse of the grid point $N$ along the interface.

Case 2 is high Reynolds flow, and is computed on 4 meshes: $32 \times 32$, $64 \times 64$, $128 \times 128$, and $256 \times 256$. On small meshes, the concentration profile exhibits oscillations around the exact solution (see Fig. 5), which is a clear sign of under-resolution of the problem [5]. The convergence of our method is shown in Fig. 4 by the '$\times$' symbol, where the solution computed on the $256 \times 256$ mesh is used as the reference solution. It appears to be better than first order convergence as the above oscillations disappear from the $128 \times 128$ mesh. In both cases, the numerical difficulty is caused by the singularity of the concentration profile. However, the singularity point is one dimension lower than the interface, and the first order convergence on the profile does not greatly affect the global accuracy of the method over the whole system. We have compared the bubble shapes computed on different meshes for case 1 (not shown here), and can hardly discern any difference between them once the mesh is larger than $32 \times 32$. Bubble deformation is quantitatively characterized in term of the Taylor deformation number $D = (l - b)/(l + b)$, where $l$ is the bubble half-length and $b$ its radius at the midsection. Table 1 records the Taylor deformation numbers and the corresponding mesh sizes. It shows that using a $64 \times 64$ mesh, we are able to compute the first three digits of the Taylor deformation number accurately.

We have also checked our computation against the analytical stagnant cap solution of a rising bubble and the final rising speed we obtained agrees well with the analytical value [2], with less than 5% difference. This difference may be due to the effects of inertia and the far field boundary condition used in our code. It is of importance to compare our results with corresponding ones obtained by very different approaches, and all the above checks lead us to believe that our numerical methods are accurate and reliable.

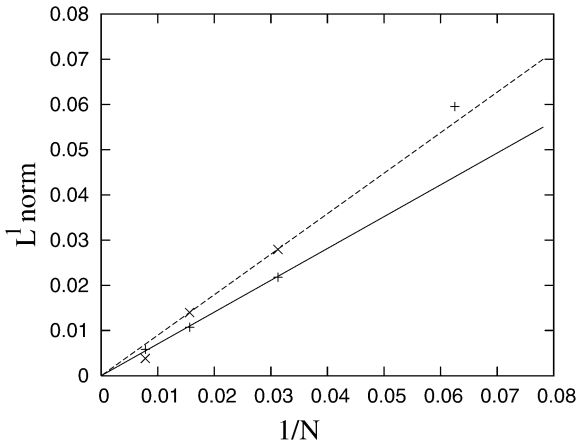


Fig. 4. First order convergence of the concentration profile based on $L^1$ norm. The '+' symbol represents the $L^1$ norm error as function of the inverse of the number of grid points $N$ on the interface for $Re = 10$, $We = 0.5$ and $x = 0.1$, while the solid line represents first order convergence. The '$\times$' symbol represents the $L^1$ norm error for $Re = 1000$, $We = 0.5$ and $x = 0.01$, and the dashed first order convergence.

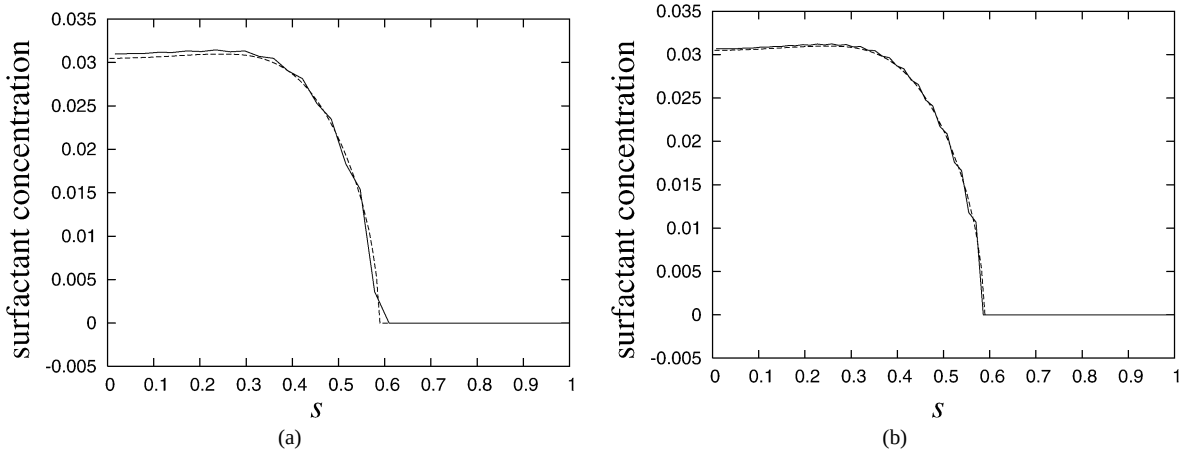


Fig. 5. Solid lines show oscillations of the concentration profile computed on small meshes (a) $32 \times 32$, and (b) $64 \times 64$. The dashed line represent the profile on a $128 \times 128$ mesh, where no oscillation is seen.

Table 1
Taylor numbers and the corresponding Mesh sizes. $Re = 10$, $We = 0.5$ and $x = 0.1$

| Mesh size | $32 \times 16$ | $32 \times 32$ | $64 \times 64$ | $64 \times 128$ | $64 \times 256$ |
|---|---|---|---|---|---|
| $D$ | 0.195314 | 0.19383 | 0.192249 | 0.192114 | 0.192082 |

## 5. Results

In this section, we discuss our numerical simulations and characterize the effects of surfactants on the bubble deformation. We investigate flows from moderate Reynolds numbers, $Re = 10$ to high Reynolds number up to $Re = 1000$. We focus on new findings related to the importance of boundary conditions and the role of inertia. As a practical matter, we fix the equilibrium bubble radius $a = 0.5$, and the principal strain rate $G = 1.0$. In order to obtain the desired Reynolds and Weber numbers, we choose the appropriate liquid viscosity $\mu$ and equilibrium surface tension $\gamma_0$. Constant $R$ and $T$ in Eq. (1) are chosen such that the *Elastic* number $E = 0.2$. In the following sections, the physical quantities will be presented in their dimensional values instead of their dimensionless values. In fact, in all our arguments, we only compare the relative order of the physical quantities between different regimes.

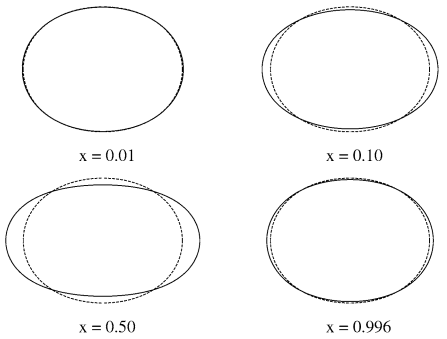


Fig. 6. Steady bubble shapes placed in a uniaxial flow. $Re = 10$ and $We = 0.5$. The solid lines represent bubbles for $x = 0.01$, 0.10, 0.50, and 0.996, and the dashed line the clean bubble.

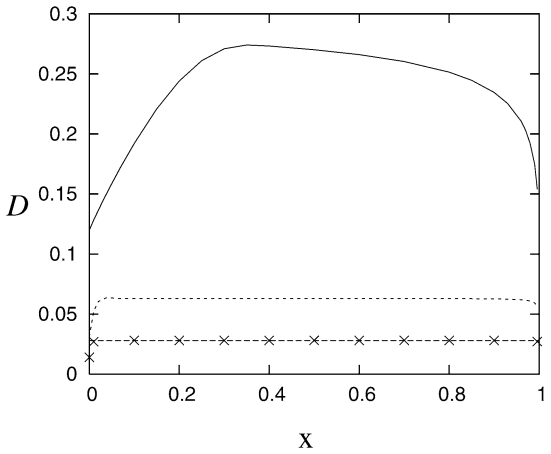


Fig. 7. Deformation $D$ vs. surface coverage. The solid line represents the Reynolds number $Re = 10$ and the Weber number $We = 0.5$, and the $\times$ symbol represents the Reynolds number $Re = 1000$ and Weber number $We = 0.5$. The value of the dashed line is 0.028. The deformation is nearly constant for unclean bubbles at $Re = 1000$, and the deformation of a clean bubble is just half this. The dotted line represents the Reynolds number $Re = 1000$ and Weber number $We = 1.0$.

### 5.1. Observations

We first present our simulations in detail for the Reynolds number $Re = 10$ and the Weber number $We = 0.5$. Fig. 6 shows the steady bubble shapes for different surface coverage of surfactant. We consider the shape of a clean bubble ($x = 0.00$) as a reference shape (dashed lines). The bubble shapes for other surface coverages (solid lines) are compared to that of the clean bubble. For the dilute concentration ($x = 0.01$), the bubble is only slightly more deformed than the clean bubble, while the deformation for $x = 0.50$ is the highest. However, the bubble deformation does not increase monotonically with the increase of surfactant concentration. For a high concentration $x = 0.996$, the bubble deformation is in fact significantly reduced. A complete picture of the bubble deformation is shown Fig. 7, where the solid represents the deformation number $D$ as a function of the equilibrium concentration $x$ for $Re = 10$ and $We = 0.5$.

It is revealing to examine the surfactant concentration profile and the surface velocity along the interface. Fig. 8 shows the surfactant concentration profiles as a function of the arclength, for surface coverage $x = 0.01$, 0.10, 0.50 and 0.996. The solid lines represent the steady profiles, while the dashed lines represent the initial profile. At low surface coverages ($x = 0.01$ and 0.10), the bubble is divided into two clear-cut regions: the surfactant accumulates near the bubble tip where the concentration is higher than the initial one, while the region close to the equator is free of surfactant. For high surface coverages ($x = 0.50$ and 0.996), the whole bubble surface is covered with surfactant. We note that the larger the surface coverage, the smaller the concentration gradient at the final state. This is explained as follows. The external viscous stress is of the same order for the same flow condition, and so also must be the surface tension gradient which balances it. However, the surface tension gradient reads:

$$\frac{\partial \gamma}{\partial s} = \frac{RT}{1-x}\frac{\partial \Gamma}{\partial s} = \frac{\gamma_0 E}{1-x}\frac{\partial x}{\partial s}. \tag{24}$$

The larger the surface concentration $x$ is, the smaller its gradient must be. Consequently, at the concentration $x = 0.996$, the concentration is nearly uniform (small gradient). As the total amount of surfactant is conserved and the surface area is increased, the concentration in a steady state is everywhere smaller than the its initial value for $x = 0.996$ (Fig. 8).

Fig. 9 shows the tangential velocity profiles for $x = 0.00$, 0.01, 0.10, and 0.50. For the clean bubble ($x = 0.00$), the tangential velocity is zero only at the equator and the tip, and the liquid flows freely along the bubble surface. For $x = 0.01$, we observe a small immobile zone (where the tangential velocity is zero) close to the tip. This is exactly the region where the surfactant concentration is not zero. As we increase the surface coverage ($x = 0.1$), the corresponding immobile zone increases, and at $x = 0.5$, the whole bubble surface becomes immobile. In all these cases, the numerical value of the velocity in our solution is below $10^{-6}$ in the immobile region (where the surfactant concentration is not zero). The foregoing two figures show clearly that our steady solutions are strict stagnant cap solutions. This is only possible when the surface diffusivity is zero.

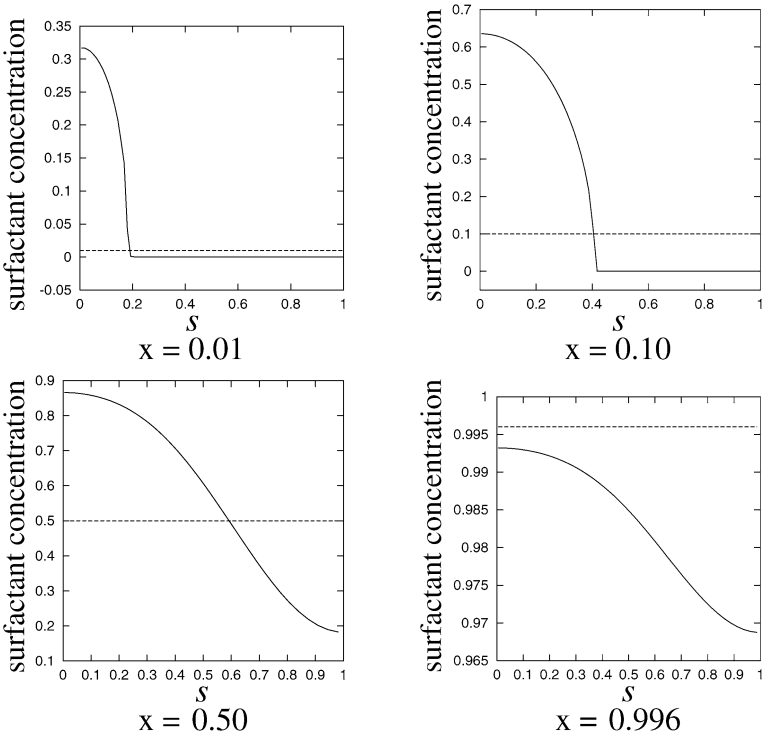


Fig. 8. Surfactant concentration along the interface. $Re = 10$ and $We = 0.5$. The surfactant concentrations are $x = 0.01$, 0.10, 0.50 and 0.996. The solid lines represent the final profiles and dashed lines the initial profiles.

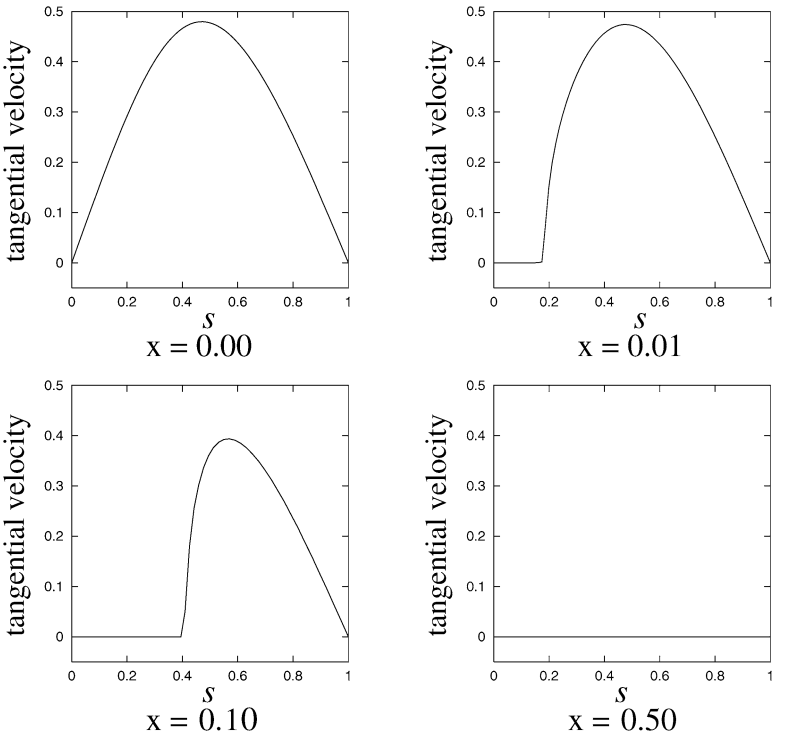


Fig. 9. Tangential velocity along the interface. The surfactant concentrations are $x = 0.00$, 0.01, 0.10, and 0.50. $Re = 10$ and $We = 0.5$.

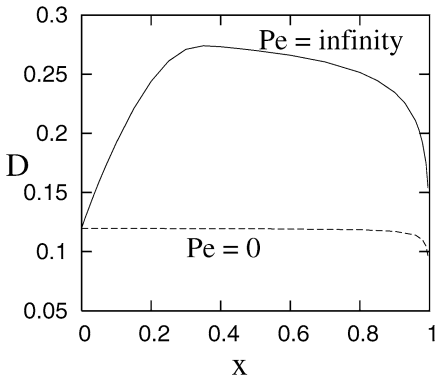


Fig. 10. Deformation $D$ vs. surface coverage for different Péclet number. The solid line represents the deformation at $Pe_s = \infty$ and the dashed line at $Pe_s = 0$. $Re = 10$ and $We = 0.5$. The deformation will lie between these two curves for finite but not zero Péclet number.

### 5.2. From slip to non-slip conditions: increase of skin friction

This work is to investigate the limit case of zero surface diffusivity $Pe_s = \infty$. It is however helpful to discuss the opposite (diffusion dominant) case $Pe_s = 0$, where the surface tension is always spatially uniform (but time-dependent) on the whole bubble surface. As consequence, the boundary condition is a *free-slip condition*. We note that when a bubble is stretched (its surface area increases), the surface tension does not change for a clean bubble $x = 0$ while it does increase for an unclean bubble. And, by definition, if the Weber number is the same, the initial value of the surface tension $\gamma_0$ is the same regardless of the initial surface concentration, which of course implies that the corresponding two pure liquids are different. From the above observations, we can deduce that a clean bubble (smaller surface tension in the final state) will deform more than an unclean bubble. This is shown in Fig. 10(a) (the dashed line) for $Re = 10$ and $We$ where the decrease of the deformation at the high concentration end is prominent.

Now we are ready to discuss a new phenomenon we have observed for the case $Pe_s = \infty$. For the sake of comparison, we plot the deformation curve in Fig. 10(a) (the solid line) for the same Reynolds and Weber numbers. The surface tension profiles corresponding to Fig. 8 are computed according to Eq. (1) and shown in Fig. 11. The solid lines represent the steady profiles, while the dashed lines represent the initial surface tensions, which all have the same value 0.5. We note that for $x = 0.996$, the surface tension in the final steady state is everywhere larger than the initial equilibrium surface tension (consistent with the concentration profile), and is therefore larger than that of a clean bubble with the same Weber number. We would expect that for the same flow condition, this bubble (with larger surface tension in the final state) will deform less than a clean bubble. However, Fig. 10(a) shows just the contrary; the deformation is higher at the high concentration $x = 0.996$ ($D = 0.154$) than the clean bubble ($D = 0.120$). In comparison with the case $Pe_s = 0$, we have observed a new phenomenon in high concentration regimes: larger surface tension, but also larger deformation. This observation is in general true for the other Weber numbers we studied. For all surface coverages considered in this work, the bubble deformation curves fall above the reference curve of the clean bubble.

What happens here is that the surface tension gradient generates a tangential stress which does not exist in the uniform situation $Pe_s = 0$, and this gradient is in turn responsible for an extra deformation. We can also consider this phenomenon from the point of view of boundary conditions. When the Péclet number rises from 0 to $\infty$, the boundary condition will undergo transition from the free-slip to the non-slip boundary conditions. The bubble surface is slippery when the free-slip condition applies ($Pe_s = 0$). It becomes rigid when the no-slip condition applies ($Pe_s = \infty$), and thus the liquid flow can 'grip' it, increasing the distorting force.

### 5.3. Effect of the inertia and flow separation

In this subsection, we explore flows in high Reynolds number regimes, where we might expect the formation of thin boundary layers and flow separation when the no-slip condition applies. In uniaxial flow around a bubble as shown in Fig. 12(a), the fluid accelerates from the equator, then retards round the tips; the bubble tips and equator are stagnant points (represented by black circles). These stagnant points are pressure maxima, according to Bernoulli's theorem. The velocity is non-zero in between, and thus the pressure is smaller there. When the bubble is covered partially or fully with surfactant, the no-slip condition applies on the contaminated zone of the surface close to the tips. There will be a thin boundary layer at high Reynolds numbers. Inside this layer the pressure will be similar to the pressure outside this layer, while the fluid speeds are slow. The pressure field cannot be balanced by the acceleration inside the boundary layer, as happens outside the boundary layer. Because of a rising

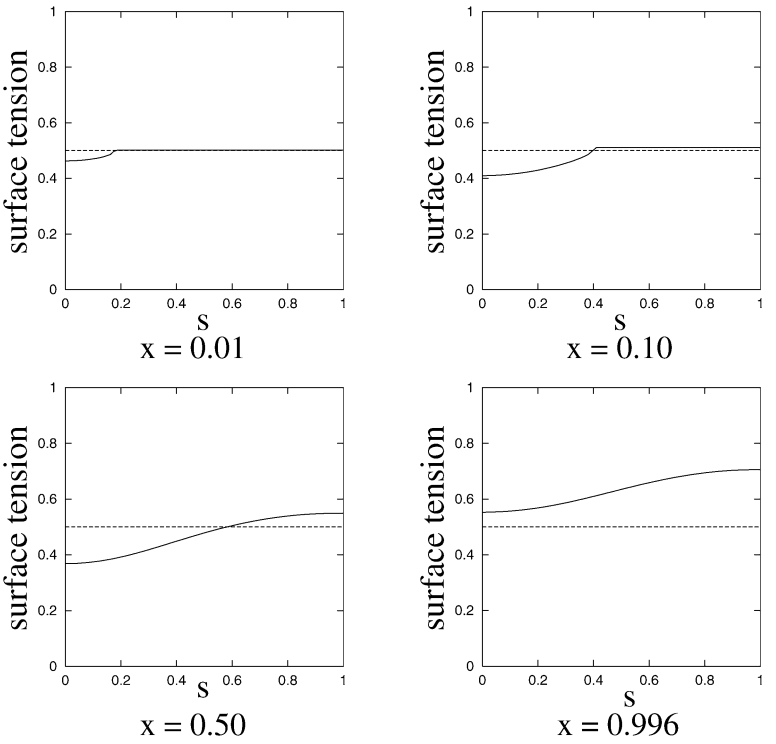


Fig. 11. Local surface tension along the interface. $Re = 10$ and $We = 0.5$. The surfactant concentrations are $x = 0.01$, 0.10, 0.50 and 0.996. The solid lines represent the final profiles and dashed lines are initial profiles.

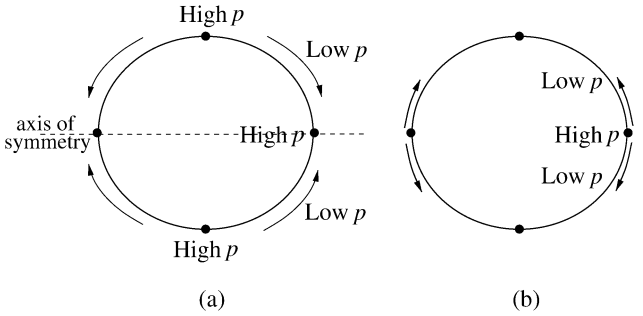


Fig. 12. Uniaxial flow around a bubble: the dashed line is the axis of symmetry. (a) The pressures and velocities outside the boundary layer. (b) The pressure-induced secondary flow near the surface of an unclean bubble.

pressure toward the axes of symmetry, there is a tendency for a reverse (secondary) flow inside the boundary layer, as shown in Fig. 12(b) and ultimately for flow separation. This mechanism of flow separation is similar to those of flows passing a cylinder or a sphere [17].

Separation of a flow passing a solid sphere may occur at Reynolds number as low as $Re = 21$. However, we only observed flow separation of the uniaxial flow at much higher Reynolds numbers, starting between 400 and 500 in our simulations. This is illustrated in Fig. 13 by the flow streamlines around the bubble, where the no-slip condition is a result of an equilibrium concentration $x = 0.01$. For $Re = 400$, the flow follows the bubble interface, while for $Re = 500$ a minor recirculation occurs at the bubble tip and the flow separates from the bubble. As the Reynolds number increases, the recirculation zone grows. In this figure, the bubbles are partially covered with surfactant. The transition zones between the free-slip and non-slip conditions are indicated by dashed circles. The streamlines exhibit sudden expansions across the singularity points. The experience of flow separation closest to this situation we know is demonstrated in plate 7 in Batchelor [17], which exhibits a transition from a

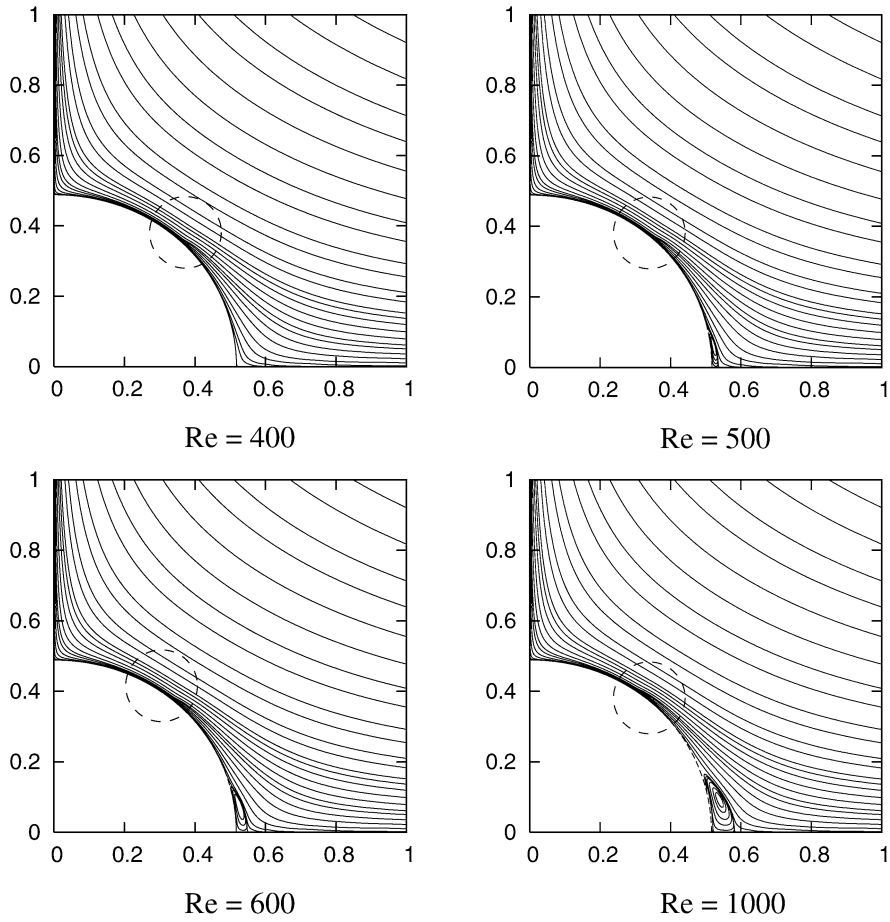


Fig. 13. Streamlines of uniaxial flow around a bubble for different Reynold numbers. The Weber number $We = 0.5$ and the equilibrium concentration $x = 0.01$. Separation occurs at $Re = 500$. Dashed circles indicate the zone of transition from the slip to the no-slip conditions.

free-slip to a no-slip condition on the symmetry plane because of the presence of a solid plate. The Reynolds number appears to be very high as there are several eddies in the recirculation zones, which seem non-stationary.

We investigate in detail the effect of the surfactant concentration at Reynolds number $Re = 1000$. Streamlines of additional uniaxial flows around the bubbles are shown in Fig. 14. The relevant profiles of the surfactant concentration is plotted as a function of the arclength in Fig. 15. The surface coverages are $x = 0.01$, 0.10, 0.50 and 0.996. The first picture in Fig. 14 concerns a clean bubble where the boundary condition is a free-slip condition. We observe no flow separation from the bubble surface. The other three diagrams are bubbles fully covered with surfactant, where the non-slip condition applies on the whole surface. The flow is separated from the bubble surfaces and the recirculation zones occur near the tips. The size of their recirculation zones is similar, but slightly smaller than that of the partially covered bubble for the same Reynolds number $Re = 1000$ in Fig. 13. Compared to Fig. 8, the maxima of the concentration profiles are no longer at the bubble tips (arclength $s = 0$), but shifted towards the equator. This is consistent with the existence of a recirculation zone; as the viscous stress changes sign, so must the concentration gradient if the boundary condition is to be satisfied.

In order to provide a global picture of the effect of inertia, we show in Fig. 16 the deformation number $D$ against the Reynolds number $Re$ for a fixed Weber number $We = 0.5$. The surface coverages considered are $x = 0.00$, 0.01, 0.10, 0.50, and 0.996. One notices that the bubble deformation decreases dramatically when $Re < 100$. Beyond $Re = 100$, the variation in bubble deformation is small. Furthermore, the deformation numbers are of similar values for unclean bubbles at high Reynolds number, despite large variations in the surface concentration. Different characteristics of the bubble dynamics between low and high Reynolds numbers are demonstrated graphically in Fig. 7, where we compare the bubble deformation number $D$ as a function of the surface coverage for the same Weber number $We = 0.5$. For the low Reynolds number $Re = 10$, the bubble deformation first increases with the surfactant concentration, then decreases. For $Re = 1000$, the deformation is roughly the

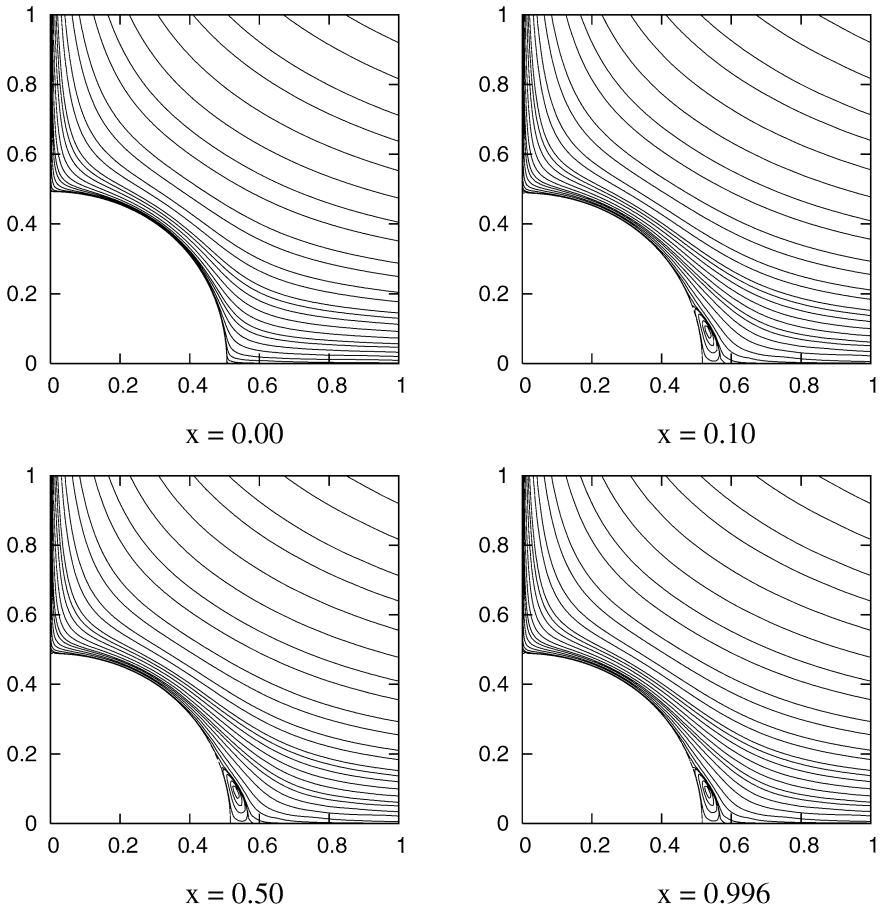


Fig. 14. Streamlines of uniaxial flow around a bubble for different surfactant concentrations. $Re = 1000$ and $We = 0.5$. The surfactant concentrations are $x = 0.00$, 0.01, 0.10, and 0.50. Separation occurs for unclean bubbles.

same, at around 0.028 for all unclean bubbles, from the dilute regime $x = 0.01$ to the high concentration regime $x = 0.996$. The deformation ($D = 0.014$) of a clean bubble is just half of that value.

## 6. Conclusions

We have studied the effect of surfactant on bubble deformation in a uniaxial flow of Reynolds number from $Re = 10$ to 1000. The relation between surfactant concentration and surface tension is a non-linear Langmuir state equation. Only an insoluble surfactant is considered. Our numerical method uses an ALE formulation based on primitive variables $u$, $v$ and $p$. The boundary conditions are naturally incorporated in this formulation and accurately resolved. In this work, the surface diffusivity of surfactants is neglected, and inertial forces are included.

Bubble deformation in the high concentration regime can be easily understood for two limiting cases, $Pe_s = 0$ and $Pe_s = \infty$. Fig. 10(a) shows an example for $Re = 10$ and $We = 0.5$, where the solid line represents the deformation at $Pe_s = \infty$ and the dashed line at $Pe_s = 0$. When the Péclet number $Pe_s = 0$ (diffusion dominant), the surface tension is uniform on the whole bubble surface, and a free-slip condition applies. This is the same boundary condition as for a clean bubble. On the other hand, the bubble surface area increases due to deformation and so does the surface tension, because the local surfactant concentration has to decrease for the total amount of surfactant to be conserved. The bubble deformation is therefore smaller than that of a clean bubble. In another extreme case where $Pe_s = \infty$ (convection dominant), both the bubble deformation and the surface tension are larger than that of a clean bubble in the high concentration regime. What happens here is that the surface tension gradient generates a tangential stress which does not exist in the uniform situation $Pe_s = 0$, and this gradient is in turn responsible for an extra deformation.

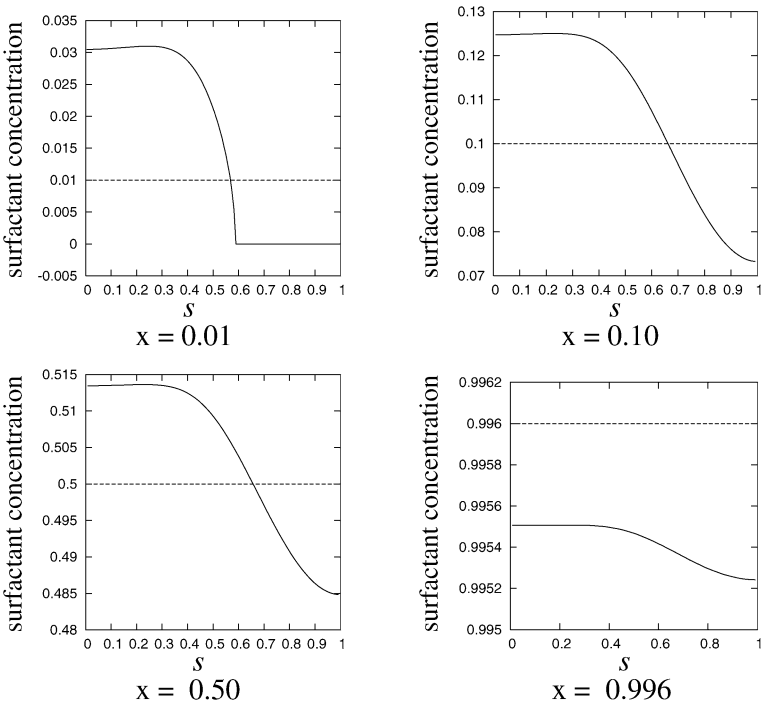


Fig. 15. Surfactant concentration along the interface. $Re = 1000$ and $We = 0.5$. The surfactant concentrations are $x = 0.01$, 0.10, 0.50 and 0.996. The solid lines represent final profiles and dashed lines initial profiles. The bubble is only partially covered for $x = 0.01$.

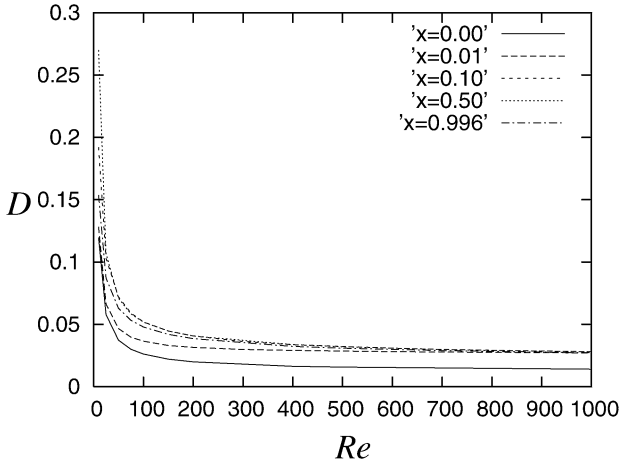


Fig. 16. Deformation $D$ vs. $Re$ for $x = 0.00$, 0.01, 0.10, 0.50, and 0.996. Weber number $We = 0.5$.

Finally, we investigate the role of the inertia at high Reynolds numbers, where the no-slip condition leads to new phenomena: the formation of boundary layers and flow separation. We find that the bubble deformation decreases dramatically when $Re < 100$. Beyond $Re = 100$, the variation in bubble deformation is small, despite more complex flow patterns. At high Reynolds number $Re = 1000$, the bubble deformation tends to take approximately one single value for a large range of surface coverage as result of the no-slip boundary condition.

Despite considering an insoluble and non-diffusing surfactant, the relevant parameter space is large for this problem. For this reason we have not conducted a complete parametric study. Furthermore, the limit of an insoluble surfactant excludes the exchange of surfactant between the bubble surface and the bulk liquid, and therefore a rich class of physical mechanisms. This should be relaxed in future work. By no means does this work attempt to be comprehensive, but a step forward towards new

understandings of the surfactant effect. Considerably more work is necessary before the complex effects of surfactant on bubble dynamics will be fully understood.

**Acknowledgement**

We would like to thank Dr. D. Lyness and Dr. D. Pritchard for proofreading the manuscript.

**References**

[1] Y. Amarouchene, G. Cristobal, H. Kellay, Noncoalescing drops, Phys. Rev. Lett. 87 (20) (2001) 206104.
[2] S.S. Sadhal, R.E. Johnson, Stokes flow past bubbles and drops partially coated with thin films. Part I. Stagnant cap of surfactant films: Exact solution, J. Fluid Mech. 126 (1983) 237.
[3] B. Cuenot, J. Magnaudet, B. Spennato, The effects of slightly soluble surfactants on the flow around a spherical bubble, J. Fluid Mech. 339 (1997) 25–53.
[4] Y.P. Wang, D.T. Papageorgiou, C. Maldarelli, Increased mobility of a surfactant-retarded bubble at high bulk concentrations, J. Fluid Mech. 390 (1999) 251–270.
[5] R.L. Sani, P.M. Gresho, Incompressible Flow and the Finite Element Method, vol. 2, Wiley, 2000.
[6] G. Ryskin, L.G. Leal, Numerical solution of free-boundary problems in fluid mechanics. Part 3: Bubble deformation in an axisymmetric straining flow, J. Fluid Mech. 148 (1984) 37–43.
[7] H.A. Stone, A simple derivation of the time-dependent convective-diffusion equation for surfactant transport along a deforming interface, Phys. Fluids A 2 (1) (1990) 111–112.
[8] H.A. Stone, L.G. Leal, The effects of surfactants on drop deformation and breakup, J. Fluid Mech. 220 (1990) 161.
[9] R. Scardovelli, S. Zaleski, Direct numerical simulation of free surface and interfacial flow, Ann. Rev. Fluid Mech. 31 (1999) 567–604.
[10] Y. Renardy, M. Renardy, V. Cristini, A new volume-of-fluid formulation for surfactants and simulations of drop deformation under shear at a low viscosity ratio, Eur. J. Mech. B Fluids 21 (2002) 49–59.
[11] M.A. Drumright-Clarke, Y. Renardy, The effect of insoluble surfactant at dilute concentration on drop breakup under shear with inertia, Phys. Fluids 16 (1) (2004) 14–21.
[12] A.J. Chorin, A numerical method for solving incompressible viscous flow problems, J. Comput. Phys. 2 (1967) 12–26.
[13] J. Li, Numerical resolution of Navier–Stokes equation with reconnection of interfaces. Volume tracking and application to atomization, PhD thesis, University of Paris VI, 1996.
[14] R.J. Leveque, Numerical Methods for Conservation Laws, Birkhäuser, 1992.
[15] M. Hesse, Numerical simulation of axi-symmetric rising bubbles, Master thesis, University of Cambridge, 2003.
[16] G. Ryskin, L.G. Leal, Numerical solution of free-boundary problems in fluid mechanics. Part 2: Buoyancy-driven motion of a gas bubble through a quiescent liquid, J. Fluid Mech. 148 (1984) 19–36.
[17] G.K. Batchelor, An Introduction to Fluid Dynamics, Cambridge University Press, 1970.